

Classification of modes in suspended-membrane, 19-missing-hole photonic-crystal microcavities

Wan Kuang, Jiang R. Cao, Tian Yang, Sang-Jun Choi, Po-Tsung Lee, John D. O'Brien, and P. Daniel Dapkus

*Electrical Engineering-Electrophysics, University of Southern California, Powell Hall of Engineering,
3737 Watt Way, Los Angeles, California 90089*

Received August 30, 2004; revised manuscript received December 1, 2004; accepted December 7, 2004

Suspended-membrane 19-missing-hole microcavities in triangular lattice photonic crystals are numerically modeled by a three-dimensional finite-difference time-domain method. The resonance frequencies and the quality factors are calculated by interpolation of the discrete Fourier transformation series of the field with a Padé polynomial. The numerical results are compared with the photoluminescent spectra measured on the cavity of a nearly identical dimension. The symmetry properties of the defect modes are analyzed with the group theory, and resonance modes in the photonic-crystal cavities are identified as irreducible representations of the C_{6v} point group. The far-field radiations of the identified modes in the free space are also calculated by use of a vector Green's function. It is found that the numerical results agree very well with the experimental measurement in various aspects. © 2005 Optical Society of America

OCIS codes: 230.3990, 140.3460.

1. INTRODUCTION

Modes in photonic-crystal laser cavities can be engineered in some detail through patterning of the local dielectric environment on a subwavelength scale. To take advantage of this ability to engineer the laser modes, one must demonstrate that experimentally observed modes agree with theoretical predictions. Because the first single-defect microcavity¹ on a triangular-lattice photonic crystal has a fairly low quality factor for resonance modes in the photonic bandgap, researchers have focused on other cavity designs, including modified single-defect^{2,3} and larger-defect cavities.^{3,4} Recently, there have been reports of high- Q modified single-defect microcavities on graded triangular-lattice photonic crystals.⁵ Unlike a traditional defect cavity usually with one hole or multiple holes removed from the lattice, those cavities are generally created by an increase of the hole radius of the defect and a careful arrangement of the hole radii of the adjacent holes. When the defect hole radius over the photonic crystal lattice is changed, the dielectric band mode is pulled into the photonic-crystal bandgap. When the hole radii of the photonic crystal cladding, is radially changed the purpose of minimizing the k -space overlap of the field with the radiation light cone is fulfilled. In this work, we focus on resonant cavities formed when three concentric rows of holes are removed. The resulting cavity is $\sim 2.5 \mu\text{m}$ across. There are three reasons motivating our efforts on these slightly larger cavities. First, these cavities often have a larger optical confinement factor than the modified single-defect cavities, since the modified single-defect modes generally peak at the locations where dielectric gain material has been removed. Because the threshold modal gain is inversely proportional to the product of the quality factor and confinement factor,

$$g = \frac{2\pi\bar{n}}{\lambda_0} \frac{1}{Q\Gamma}, \quad (1.1)$$

in which Γ is the optical confinement factor indicating the percentage of the field overlap with the gain medium, g is the threshold material gain, \bar{n} is the effective index for the resonance mode at the wavelength λ_0 , and Q is the mode quality factor, it is useful to consider the trade off between quality factor and confinement factor. This trade-off is especially true, since little is known about the spatial dependency of the gain near the etched photonic-crystal sidewalls. Second, the manufacturing tolerance for these slightly larger cavities is relaxed. Finally, electrically pumped photonic-crystal cavities may contain an oxide aperture whose minimum radius is likely to be limited to 2–3 μm by electrical resistance.

However, a detailed numerical analysis on such multi-mode cavities can be a difficult problem, since there can be many closely spaced modes in these larger cavities. In this paper, numerical methods are introduced for efficient characterization of multimoded photonic-crystal microcavities. It is shown that we obtained excellent agreement between our numerical predictions and the observed modes. The paper is organized as follows. Section 2 presents the results of a three-dimensional (3-D) finite-difference time-domain (FDTD) simulation. As a part of quality-factor calculation, a time-domain discrete Fourier transform (DFT) of the magnetic field component H_z at low-symmetry locations of the cavity is interpolated with Padé polynomials. The quality factors are then calculated by the full width at the half magnitude of each resonance peak in the Padé interpolated frequency response. Experimental data in the form of photoluminescence (PL) spectra from the fabricated devices are also given and com-

Report Documentation Page

Form Approved
OMB No. 0704-0188

Public reporting burden for the collection of information is estimated to average 1 hour per response, including the time for reviewing instructions, searching existing data sources, gathering and maintaining the data needed, and completing and reviewing the collection of information. Send comments regarding this burden estimate or any other aspect of this collection of information, including suggestions for reducing this burden, to Washington Headquarters Services, Directorate for Information Operations and Reports, 1215 Jefferson Davis Highway, Suite 1204, Arlington VA 22202-4302. Respondents should be aware that notwithstanding any other provision of law, no person shall be subject to a penalty for failing to comply with a collection of information if it does not display a currently valid OMB control number.

1. REPORT DATE 01 JUN 2005	2. REPORT TYPE N/A	3. DATES COVERED -	
4. TITLE AND SUBTITLE Classification of modes in suspended-membrane, 19-missing-hole photonic-crystal microcavities		5a. CONTRACT NUMBER	
		5b. GRANT NUMBER	
		5c. PROGRAM ELEMENT NUMBER	
6. AUTHOR(S)		5d. PROJECT NUMBER	
		5e. TASK NUMBER	
		5f. WORK UNIT NUMBER	
7. PERFORMING ORGANIZATION NAME(S) AND ADDRESS(ES) Electrical Engineering-Electrophysics, University of Southern California, Powell Hall of Engineering, 3737 Watt Way, Los Angeles, California 90089		8. PERFORMING ORGANIZATION REPORT NUMBER	
		10. SPONSOR/MONITOR'S ACRONYM(S)	
9. SPONSORING/MONITORING AGENCY NAME(S) AND ADDRESS(ES)		11. SPONSOR/MONITOR'S REPORT NUMBER(S)	
		12. DISTRIBUTION/AVAILABILITY STATEMENT Approved for public release, distribution unlimited	
13. SUPPLEMENTARY NOTES See also ADM001923.			
14. ABSTRACT			
15. SUBJECT TERMS			
16. SECURITY CLASSIFICATION OF:			17. LIMITATION OF ABSTRACT
a. REPORT unclassified	b. ABSTRACT unclassified	c. THIS PAGE unclassified	UU
			18. NUMBER OF PAGES 8
			19a. NAME OF RESPONSIBLE PERSON

pared with the calculation. In Section 3, the field distributions for the resonant modes of interest are obtained by application of a digital filter during the FDTD simulation. The resonant modes are classified in the C_{6v} point-symmetry group by projection of the electrical and magnetic fields onto irreducible representations of the group. The modes are invariant under the set of symmetry operations of the irreducible representations of the relevant point group. Section 4 presents the free-space far-field radiation pattern of a doubly degenerate resonant mode calculated with the vector Green's function approach. The result is compared with the experimental measurement, which agrees very well with the theoretical analysis.

2. RESONANCE MODES AND QUALITY FACTORS

The frequency response of the cavity is calculated by a Fourier transform of the time-dependent field at the low-symmetry locations recorded from a 3-D FDTD simulation.^{6,7} However, since the dielectric constants of all of the materials are assumed to be real and constant in the simulation, we are limited to predicting the cold cavity behavior of the cavities. Since only a limited number of modes exist in such a device, the frequency resolution of the temporal Fourier transform, which is given by

$$\frac{\Delta f}{f} = \frac{M}{N(a/\lambda_0)}, \quad (1.2)$$

in which a is the lattice constant of the photonic crystal, λ_0 is the free space wavelength, N is the total number of samples for the Fourier transform, and M is the number of time steps it takes for the field to travel a distance of a in the free space, shows that the frequency resolution can be made to be much smaller than the mode spacing.

In contrast, the situation for the quality-factor calculation for the multimode cavity is more complicated. Calculation of the quality factor of each resonance by the ratio of the power exiting the device and the total energy in the cavity¹ generally requires a significant number of time steps, because it requires the use of a time-domain filter narrow enough in the frequency domain so that only the desired mode is excited. For a given filter window, the ratio of the filter bandwidth BW and its central frequency f is given by

$$\frac{BW}{f} = \frac{\pi\xi M}{N(a/\lambda_0)}, \quad (1.3)$$

where ξ is the transition width factor of equivalent Kaiser window. For example, a Hanning window has a ξ of 5.01. The spacing between modes for multimode microcavities is generally so small that an implementation of the sharp filter is impractical. The method is also somewhat sensitive to the filter efficiency and tends to be less accurate as the quality factor of the mode increases, since the lost power is very small for a high- Q resonant mode.

In this paper, because of the difficulty with efficient, narrow-bandpass digital filter, the quality factor is instead calculated from the ratio of full width at the half

magnitude of the cavity resonance in the frequency domain, $\Delta\omega$, to the center frequency ω_0 . The inherent limitation of this approach is its insufficient frequency resolution; the smallest identifiable spectral width usually cannot resolve a quality factor higher than a few hundred. Distortion to the spectrum is also introduced, because the numerical simulation terminates before the impulse response is fully evolved. This has the effect of viewing the true time-domain response through a rectangular window, which translates mathematically into the convolution of the true spectrum with a sinc function. The convolution widens the peaks in the spectrum, among other effects. This distortion can be reduced with an increase of the time-response window, but at a price of a longer simulation time. Padé interpolation addresses the problem through extrapolation of the electromagnetic field in the time domain beyond the actual simulation window.⁸ The DFT series $P(\omega_k)$ is interpolated with a Padé function, which is the ratio of an order I and an order J polynomials Q_I and D_J :

$$P(\omega_k) = \frac{Q_I(\omega_k)}{D_J(\omega_k)} = \frac{\sum_{i=0}^I \alpha_i(\omega_k)^i}{\sum_{j=0}^J \beta_j(\omega_k)^j}. \quad (1.4)$$

Assuming β_0 to be unity, coefficients α_i and β_j in Eq. (1.4) can be solved with $I+J+1$ Fourier transform samples, and a continuous Padé function interpolating the Fourier spectrum is derived. The accuracy of the frequency response is significantly improved beyond the frequency resolution of the discrete Fourier transform. By combining Padé approximation with the DFT, one can determine the quality factors of all modes in the cavity with just one FDTD simulation.

Figure 1 shows the TE_z -like (even) resonance mode frequencies and their quality factors for a triangular-lattice photonic-crystal defect microcavity, where the z direction is the epitaxial growth direction. The cavity is created in a dielectric membrane suspended in the air. The membrane has a refractive index n of 3.4 and a thickness d of 0.45 normalized against lattice constant a . The defect is formed when the three concentric circles of air holes, a total of 19 holes are filled, with dielectric. All air holes have a normalized radius of $r/a=0.33$ in the simulation, except those immediately adjacent to the cavity defect, which have a slightly smaller radius of $r/a=0.3$. For the purpose of comparison, the PL spectrum of an actual photonic-crystal defect cavity pumped below threshold is also shown in Fig. 1 as a curve. The devices were fabricated in an epitaxial layer structure consisting of a 20-nm-thick InGaAs etch-stop layer, a 60-nm sacrificing InP top layer to protect the quantum wells during the processing, and a 240-nm-thick InGaAsP layer containing four compressively strained InGaAsP quantum wells designed to emit at 1.5 μm at room temperature. The cavity dimensions are 8 μm by 10 μm , as shown in the scanning electron micrograph image in the Fig. 1 inset. In all cases, there are either six or seven periods of a triangular-lattice photonic-crystal cladding around the central defect. The fabricated devices had a lattice constant of 500 nm and an r/a value

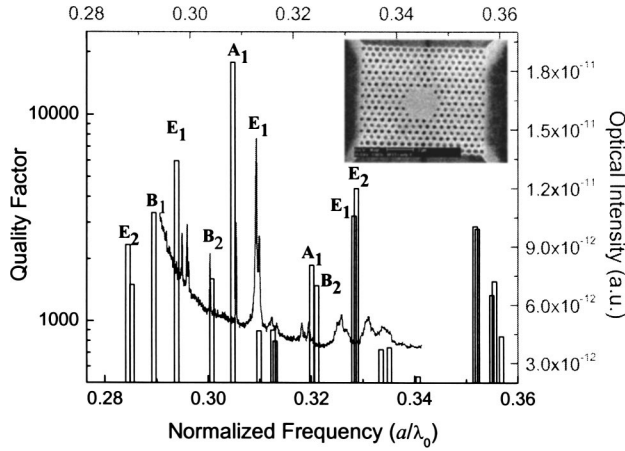


Fig. 1. Calculated resonance-mode frequencies and their quality factors for a suspended membrane 19-missing-hole photonic-crystal defect cavity (bars) with a membrane thickness of $d/a = 0.45$ and hole radii of $r/a = 0.33$ except the inner holes around the defect, which have slightly smaller $r/a = 0.3$. It is compared with the measured photoluminescent spectrum of a cavity with similar dimensions (curve). The left and bottom axes are for the calculation, whereas the right and top axes are for the measurement curve. The difference of frequency is within 0.0035 in normalized scale, or ~ 16 nm in free-space wavelength. Resonance modes with a quality factor over 1000 in the material gain region are also labeled with their corresponding irreducible representation in the C_{6v} point symmetry group. The inset shows the top view of the cavity.

of approximately 0.33. The left and bottom axes are for the calculated quality factors and the resonance frequencies, whereas the right and top axes are for the measured optical intensity and frequencies. The horizontal axes of the two plots are intentionally shifted by less than 1%, or 16 nm in wavelength. The peaks in the PL spectrum generally align very closely with the predicted resonances, except for the ones around the normalized frequency $a/\lambda_0 = 0.33$, which will be explained in Section 4. This frequency shift is attributed to the fabrication variation of the microcavity. The case in which two resonance modes are measured for the wavelength in which only one resonance is calculated is also explained in Section 4. It is worth mentioning that the lasing mode of the microcavity is the mode with the highest predicted Q at the normalized frequency of $a/\lambda_0 = 0.304$.

Notice that the PL measurement of the cavity is overlaid with the calculated quality factor of the defect modes instead of the DFT of the time evolution of the field. Because the intensity of the Fourier spectrum does not entirely reflect the photon lifetime of the resonant modes, the excitation efficiency of the initial condition with each defect mode strongly affects the magnitude of the Fourier intensity. Even though high- Q resonance has a slower energy decay in time, which results in a higher Fourier intensity at the resonance frequency given the initial energy is identical, the overlap of the random initial condition might have strongly favored low- Q modes. Additionally, the amplitude of the peaks in the PL measurement reflects the out-of-plane loss, not the total loss. The predicted high- Q modes are identified in the optical spectrum as sharper resonances, not the ones with higher optical intensity.

3. CLASSIFICATION OF RESONANCE MODES WITH GROUP THEORY

As can be seen from Fig. 1, there are usually tens of resonant modes existing for a multiple-defect photonic-crystal microcavity. Not all of the modes in the photonic bandgap are interesting. For those that do raise interest, their field distribution can be obtained with a narrow-bandwidth digital filter. The field distribution of a resonant mode provides insight into its loss mechanism. The classification of modes with the group theory provides much broader and more general information, such as degeneracy.

The TE_z -like (even) resonant modes in a 19-missing-hole suspended-membrane defect cavity belong to the irreducible representations of the C_{6v} point group.^{9,10} Table 1 shows the character table for the C_{6v} point-symmetry group. Together with the identity operation E that keeps the field as is, the C_{6v} group is composed of the following symmetry operations¹¹:

$$C_{6v} = \{E, C_2, 2C_3, 2C_6, 3\sigma_d, 3\sigma_v\}. \quad (1.5)$$

The C_{6v} point-symmetry group consists of six irreducible representations labeled as A_1 , A_2 , B_1 , B_2 , E_1 , and E_2 . A resonant mode in a 19-missing-hole photonic-crystal defect cavity assumes the property of one of the irreducible representations. For TE_z -like (even) resonance modes in the photonic-crystal microcavity, the magnetic fields are nearly scalar. In particular, the magnetic fields at the midplane of the membrane consist only of the H_z component. The vector electric field, however, is dominated by the E_x and E_y components. The symmetry operations are therefore applied to the scalar magnetic field H_z and the vector electrical field. Figure 2(a) shows the H_z component of the lasing mode at the midplane of the membrane calculated by a 3-D FDTD method with a 60,000 time-step Blackman¹² filter. Projecting this mode onto the six irreducible representations of the C_{6v} point group by applying mirror and rotation operations^{11,13} to the mode profile numerically, we obtained the projections of the scalar magnetic field component H_z onto the six irreducible representations of the C_{6v} point group. The projection operators onto the irreducible representations are given by

$$\hat{P}^{(j)} = \frac{l_j}{h} \sum_R \chi^{(j)}(R) \hat{P}_R, \quad (1.6)$$

in which \hat{P}_R is the operator corresponding to coordinates transformation R , l_j is the dimension of the j th irreducible representation, and h is the total number of elements in

Table 1. Character Table for the C_{6v} Point-Symmetry Group

C_{6v} (6mm)	E	C_2	$2C_3$	$2C_6$	$3\sigma_d$	$3\sigma_v$
A_1	1	1	1	1	1	1
A_2	1	1	1	1	-1	-1
B_1	1	-1	1	-1	-1	1
B_2	1	-1	1	-1	1	-1
E_1	2	-2	-1	1	0	0
E_2	2	2	-1	-1	0	0

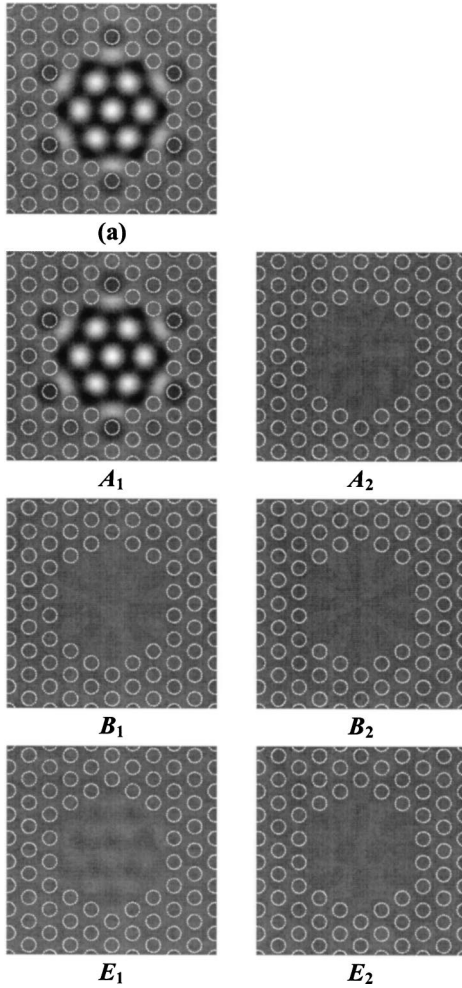


Fig. 2. Magnitude of the H_z component at the midplane for the 19-missing-hole suspended-membrane photonic-crystal defect-cavity mode considered (top), with a two-dimensional dielectric contour overlaid. Its projections onto the irreducible representations of the C_{6v} group are labeled by A_1 , A_2 , B_1 , B_2 , E_1 , and E_2 .

the group. The projections of the calculated field for the mode that lases experimentally are plotted in the same linear gray scale to emphasize the fact that the fields have a trivial amount of overlap with representations other than A_1 . Energy in projections other than A_1 account for less than 1% of the total. Additionally, the magnetic field is nearly identical before and after a set of projection operations characterizing A_1 irreducible representations. Therefore the magnetic field H_z of the lasing mode is identified as an A_1 mode of the C_{6v} point group.

The remaining projections are attributed to the inefficiency of the temporal bandpass filter and the numerical errors involved with the symmetry operations. Even though a Blackman filter has a sidelobe suppression ratio of 57 dB, some traceable amount of energy still remains after the bandpass filtering, depending on the initial excitation condition and the photon lifetime of adjacent resonant modes. In addition, the rotations and the mirror reflections of the multiples of 60 deg cannot be implemented in the Cartesian coordinates without the application of antialiasing. Here, we have applied a weighted

nearest-neighbor approach for the values that is not directly given by the FDTD simulation.

The remaining projection also proves a point we made in Section 2. The quality factor of a multimoded cavity calculated with the ratio of dissipated power and total energy is distorted by the remaining energy of the neighboring resonances inadequately suppressed by the time-domain filter. Even with only a fraction of a percent of energy remaining in other modes, the calculation of the quality factor cannot be accurate for modes having a quality factor larger than a few thousand. As the filter bandwidth and the sideband suppression ratio generally decrease inversely with the filter window length, given a filter window function, realization of a desirable filter is computationally cumbersome. Certainly, one can use the result after the projection operation as an initial condition for elimination of the noise from the undesired modes and acceleration of the convergence.

An additional error occurs in the projection of the vector electric field as a result of the noncollocation grid scheme employed in the FDTD simulation. Because the electric field components E_x and E_y are sampled at different spatial locations, interpolation is required for one of the field components to obtain its value on the locations where the other component is sampled. For simplicity, a linear interpolation is applied in the transformation.

Accordingly, the electric fields E_x and E_y of the same mode assume the symmetry properties of the A_2 irreducible representation of the C_{6v} group, as shown in Fig. 3. Here, we followed the projection rules elaborated by Sakoda,¹³ that is, the projections of the real vectors and pseudovectors conform to the same formula. The difference between the E and H fields originates from the fact that the electric field is a true vector, whereas the magnetic field is an axial vector. Under mirror reflections or improper rotations, the electric field behaves as

$$\mathbf{E} \rightarrow \mathbf{E}' = -\mathbf{E}, \quad (1.7)$$

whereas magnetic field behaves like

$$\mathbf{H} \rightarrow \mathbf{H}' = -\mathbf{H}. \quad (1.8)$$

The characters for irreducible representations A_1 and A_2 have opposite signs for mirror reflections σ_d and σ_v . Some other literature applies an additional negative sign to all improper rotation operations of the pseudovectors. The electric and magnetic fields therefore conform to same set of irreducible representation. In this paper, we will label the resonant mode based on the representation of its magnetic field. For resonant modes in the material gain region that spans from the normalized frequency of 0.28 to 0.34, their irreducible representations in the C_{6v} point symmetry group are labeled in Fig. 1. Even though this paper focuses on the application of group theory to identify modes calculated from FDTD, we shall point out that application of the group theory can also be used during the numerical simulation to restrict the resonant modes only to those satisfying the symmetry condition, thereby improving calculation convergence.

4. RESONANCE MODES' FAR-FIELD RADIATION

The polarization of a resonant mode can also be experimentally measured and numerically evaluated. Comparing the polarization measurement with the calculation result serves as additional confirmation of the numerical predictions.

As shown in Figs. 2 and 3, the near field of the lasing mode assumes a 60-deg rotational symmetry. It is there-

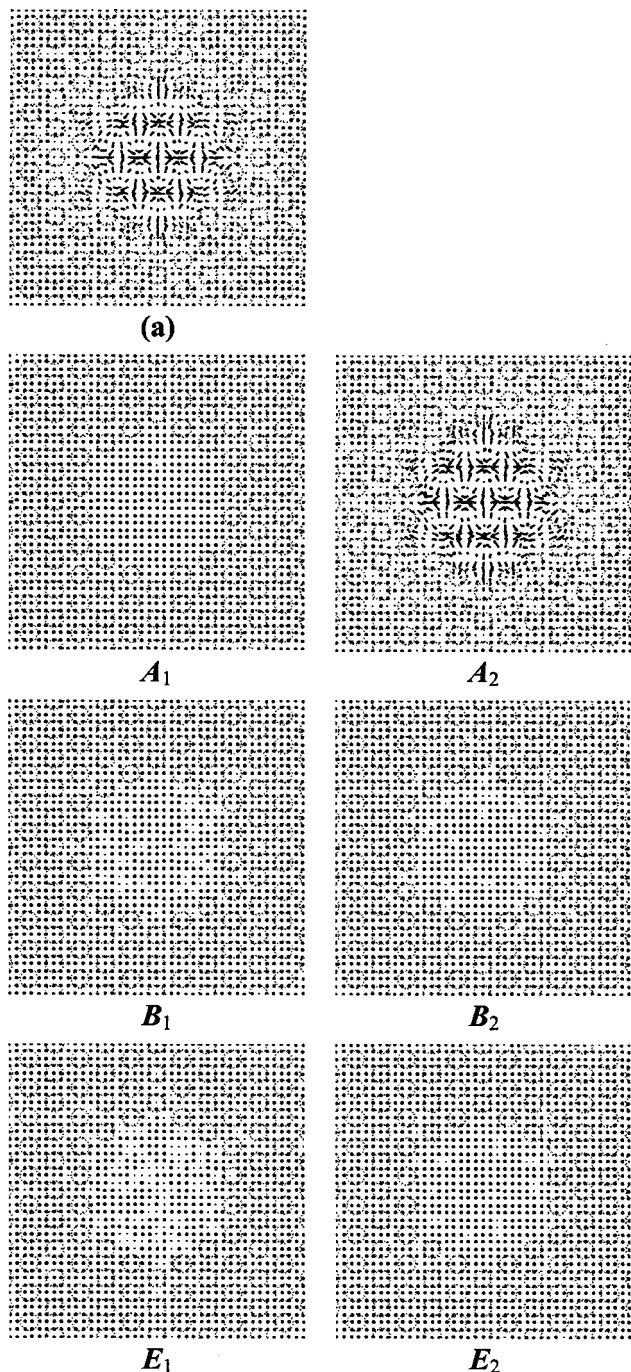


Fig. 3. Electrical-field components E_x (top left) and E_y (top right) at the midplane for the 19-missing-hole suspended-membrane photonic-crystal defect-cavity mode considered (top), with a two-dimensional dielectric contour overlaid. Their projections onto the irreducible representations of the C_{6v} group are labeled by A_1 , A_2 , B_1 , B_2 , E_1 , and E_2 .

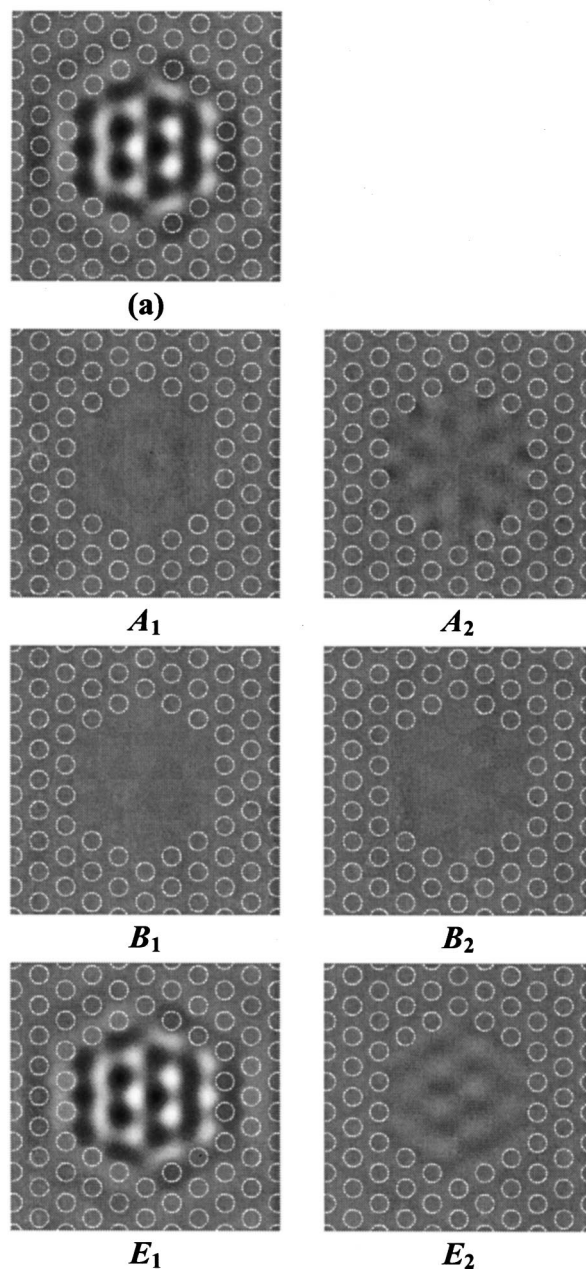


Fig. 4. Magnitude of the H_z component at the midplane for the 19-missing-hole suspended-membrane photonic-crystal defect-cavity mode considered (top), with a two-dimensional dielectric contour overlaid. Its projections onto the irreducible representations of the C_{6v} group are labeled by A_1 , A_2 , B_1 , B_2 , E_1 , and E_2 .

fore expected that the polarization of the radiation for the lasing mode is not linearly polarized. Its polarization of the radiation varies little with angle; the experimental characterization of the lasing mode is consistent with this prediction. We have also obtained agreement between the predicted spatial profile and the radiation pattern for this mode.¹⁴ More-specific agreement between prediction and polarization measurement occurs for modes at the normalized frequency of 0.309 ($\lambda_0 \sim 1618$ nm). Figure 4 shows the magnetic-field component H_z at the midplane of the microcavity. Its projections on $\{A_1, A_2, B_1, B_2, E_1, E_2\}$ of the C_{6v} point group are shown in the same linear gray scale. As with the lasing mode, the resonance af-

ter FDTD and the Blackman filter has a negligible projection onto representations other than E_1 .

As shown in Table 1, E_1 of the C_{6v} group is a two-dimensional representation, which implies that the eigenmode is doubly degenerate. For a two-dimensional representation, the final mode's spatial distribution depends on the coefficients of its two-dimensional linear combination. These coefficients depend on the initial condition. Figure 5 shows another simulation of the same E_1 mode excited with a different initial condition. Even though the field distributions in Figs. 4 and 5 are visually different, they are invariant after the same set of symmetry operations.

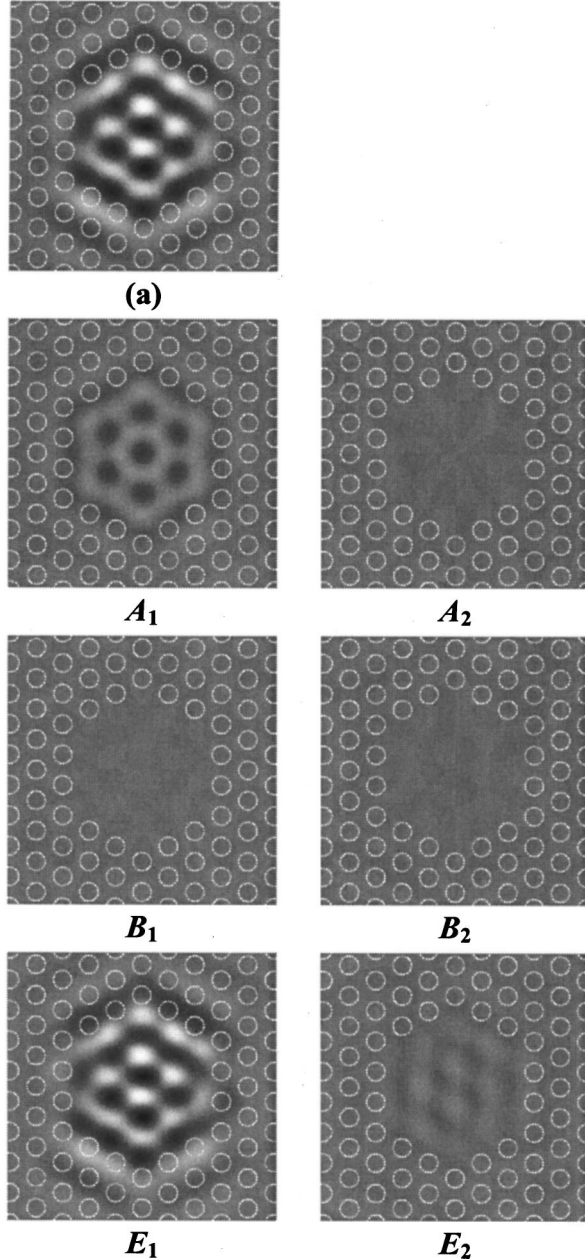


Fig. 5. Magnitude of the magnetic field H_z at the midplane (top) of the 19-missing-hole suspended-membrane photonic-crystal defect cavity for the same mode as in Fig. 5 but excited with different initial condition. Its projections onto the irreducible representations of the C_{6v} group are labeled by A_1 , A_2 , B_1 , B_2 , E_1 , and E_2 .

Table 2. Character Table for the C_{2v} Point-Symmetry Group

C_{2v} ($2mm$)	E	C_2	σ_v	σ'_v
A_1''	1	1	1	1
A_2''	1	1	-1	-1
B_1''	1	-1	1	-1
B_2''	1	-1	-1	1

The E_1 mode is usually observed experimentally as two closely spaced peaks. We attribute the degeneracy splitting to a perturbation resulting from the fabrication processes. The photonic-crystal patterns were created by electron beam lithography working in Cartesian coordinates. The lithography creates a rectangular perturbation that will lower the symmetry and result in the decomposition of E_1 into the irreducible representations of the C_{2v} point group. The C_{2v} point group consists of four one-dimensional irreducible representations A_1'' , A_2'' , B_1'' , and B_2'' , as shown in Table 2.

The fields after this decomposition are shown in Fig. 6. The E_1 mode of the C_{6v} group has zero projections on A_1'' and A_2'' . Its projections on B_1'' and B_2'' are identical regardless of the initial excitation, which is what is expected from the relations between the E_1 of the C_{6v} group and the B_1'' and the B_2'' of the C_{6v} group. Similarly, the double degeneracy of the E_2 mode of the C_{6v} group is expected to be split on to the A_1 and A_2 irreducible representations of the C_{6v} group. At the normalized frequency near 0.33, there are two doubly degenerate modes labeled as E_1 and E_2 in the Fig. 1. Even though both resonances at the frequency are displaced from the prediction owing to the fabrication variation, they are nonetheless observed experimentally as two closely spaced peaks.

The far-field radiation in the free space can be considered as an electromagnetic problem with a current or charge distribution as a source. It is often approached by dyadic Green's function,¹⁵

$$\mathbf{E}(\mathbf{r}) = i\omega\mu \int_v d^3r' \mathbf{J}(\mathbf{r}') \cdot \bar{\bar{G}}(\mathbf{r}, \mathbf{r}'), \quad (1.9)$$

where the dyadic Green's function is

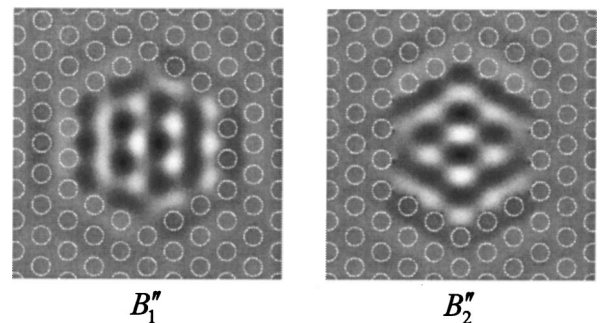


Fig. 6. Decomposition of the magnetic field H_z as shown in Figs. 5 and 6, a two-dimensional E_1 mode of the C_{6v} group, in one-dimensional representation $\{B_1'', B_2''\}$ of the C_{2v} group.

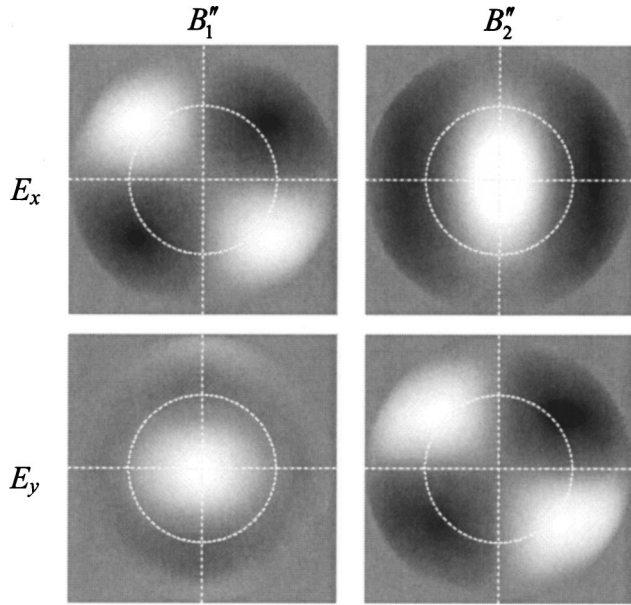


Fig. 7. Calculated E_x and E_y far-field components of the modes corresponding to the B_1'' and B_2'' representations shown in a polar plot. The dashed circle indicates a numerical aperture of 0.55, identical to the lens system employed for experimental light collection.

$$\bar{G}(\mathbf{r}, \mathbf{r}') = \left(\bar{I} + \frac{1}{k_0^2} \nabla \nabla \right) \frac{\exp(ik_0|\mathbf{r} - \mathbf{r}'|)}{|\mathbf{r} - \mathbf{r}'|}. \quad (1.10)$$

According to the uniqueness theorem, a field in a lossless region is uniquely specified by the source in it plus the tangential components of the electric field over the boundary, or the tangential components of the magnetic field over the boundary, or the tangential components of the electric field over part of the boundary and the tangential components of the magnetic field over the rest of the boundary.¹⁵ Therefore, the radiation from a locally distributed source outside the source can be calculated by equivalent surface current or charge.

$$\mathbf{E}(\mathbf{r}) = \int_s d^2r' \nabla \times \bar{G}(\mathbf{r}, \mathbf{r}') \cdot \hat{n} \times 2\mathbf{E}(\mathbf{r}'). \quad (1.11)$$

By use of the far-field approximation,

$$\left(\bar{I} + \frac{1}{k_0^2} \nabla \nabla \right) \sim (\bar{I} - \hat{r}\hat{r}), \quad (1.12)$$

the far-field radiation of each nondegenerate mode is then calculated with a vector Green's function propagation of the electric field $\mathbf{E}_s(\mathbf{r}')$ at the surface of the resonant cavity:

$$\begin{aligned} \mathbf{E}(\mathbf{r}) = & \frac{ik_0 \exp(ik_0r)}{4\pi r} \hat{r}_0 \times \iint_s -2\hat{z} \times \mathbf{E}_s(\mathbf{r}') \\ & \times \exp(-i\mathbf{k}_0 \cdot \mathbf{r}') d^2r', \end{aligned} \quad (1.13)$$

in which \mathbf{k}_0 is the free-space wave vector from the center of the defect.

Figure 7 shows the polar plots of the E_x and E_y far-field components for these two modes. The field magnitude at

the center indicates the field radiation along the optical axis. The field at the same radiation angle is shown in the plot as concentric circles. The dashed circle indicates the numerical aperture of the lens being used in the experimental system. Light emitted from the photonic-crystal microcavity is vertically collected by an optical system with a numerical aperture of 0.55. For the B_1'' mode, the E_x field goes through zero at the optical axis and the peaks of the field locate outside of the numerical aperture. The E_y field, however, peaks around the optical axis. Because the optical system can collect only a small angle of the light efficiently from the cavity, the mode appears predominantly y polarized for the lens system. In contrast, B_2'' is predominantly x polarized.

This prediction of the degenerate E_1 modes splitting into two modes that are linearly polarized along orthogonal directions was verified experimentally. Figure 8 shows the measured spectrum and the intensity of these cavity modes through a polarizer as a function of angle. The inset shows the calculated far-field radiation pattern of the respective modes. It is worth pointing out that the shapes of the far-field intensity are not the reason for determination of the polarization of the corresponding mode. The

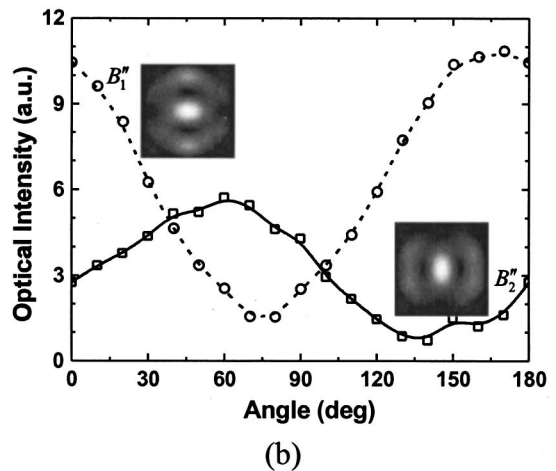
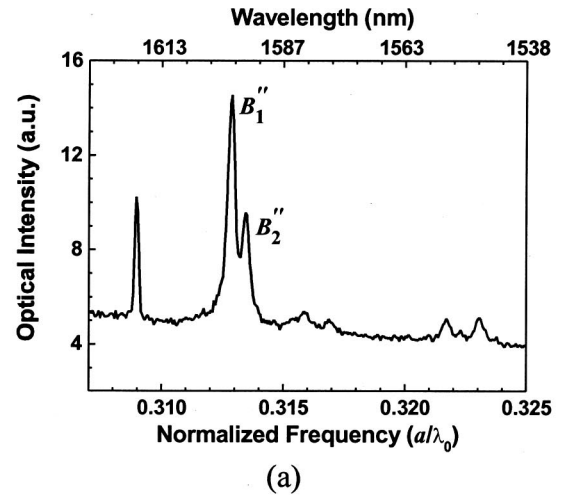


Fig. 8. (a) Measured optical spectrum of the cavity. (b) Polarizations of the two resonances split in frequency during to a rectangular perturbation of a doubly degenerate mode. The insets show the calculated far-field intensities of the respective modes.

transmitted optical power peaks as the polarizer is aligned at 170° for the B_1 mode and approximately 60° for the B_2 mode; they are nearly orthogonal. Both modes show a typical sine-squared dependency on the angle as expected for linear polarization. The peak-to-valley ratio of the optical intensity as the polarizer was rotated is about 10 for both cases.

5. SUMMARY

In summary, the resonant frequencies and the quality factors of defect modes in a 19-missing-hole suspended-membrane photonic-crystal microcavity are calculated with 3-D FDTD and Padé's approximation. Good agreement is obtained between the calculated and the measured resonant frequencies. The resonant modes are classified by the irreducible representations of the C_{6v} point group. The free-space far-field radiation patterns are calculated with the vector Green's function and are compared favorably with the polarization-resolved measurements. Although this paper has focused on a particular 19-missing-hole triangular-lattice photonic-crystal cavity, the method detailed here can be generally applied to the analysis of other multimode photonic-crystal microcavities. Even though the group theory is used to identify modes calculated from FDTD in this paper, it can also be applied in reverse. Enforcement of the symmetry properties of an irreducible representation during the numerical simulation restricts the resonant modes only to those satisfying the symmetry condition, thus allowing a wider numerical filter to be employed as the spacing between modes is generally increased, and therefore accelerating the convergence to the mode of interest.

This study is based on research supported by the National Science Foundation under grant ECS 0094020 and by the Defense Advanced Research Projects Agency under grants 10191574 and F49620-02-1-0403. Computation for the work described in this paper was supported, in part, by the University of Southern California Center for High Performance Computing and Communications.

REFERENCES

1. O. Painter, R. K. Lee, A. Yariv, A. Scherer, J. D. O'Brien, P. D. Dapkus, and I. Kim, "Two-dimensional photonic crystal defect laser," *Science* **284**, 1819–1821 (1999).
2. J. Vuckovic, M. Loncar, H. Mabuchi, and A. Scherer, "Design of photonic crystal microcavities for cavity QED," *Phys. Rev. E* **65**, 016608-1-11 (2001).
3. H.-Y. Ryu, H.-G. Park, and Y.-H. Lee, "Two-dimensional photonic crystal semiconductor laser: computational design, fabrication, and characterization," *IEEE J. Sel. Top. Quantum Electron.* **8**, 891–908 (2002).
4. P.-T. Lee, J. R. Cao, S.-J. Choi, Z. J. Wei, J. D. O'Brien, and P. D. Dapkus, "Room-temperature operation of VCSEL-pumped photonic crystal lasers," *IEEE Photonics Technol. Lett.* **4**, 435–437 (2002).
5. K. Srinivasan and O. Painter, "Fourier space design of high-Q cavities in standard and compressed hexagonal lattice photonic crystals," *Opt. Express* **11**, 579–593 (2003), <http://www.opticsexpress.org>.
6. K. S. Yee, "Numerical solution to initial boundary value problems involving Maxwell's equations in isotropic media," *IEEE Trans. Antennas Propag.* **AP-14**, 302–307 (1966).
7. A. Taflov, *Computational Electrodynamics—The Finite-Difference Time-Domain Method* (Artech House, Boston, Mass., 1995).
8. S. Dey and R. Mittra, "Efficient computation of resonant frequencies and quality factors of cavities via a combination of the finite-difference time-domain technique and the Padé approximation," *IEEE Microw. Guid. Wave Lett.* **8**, 415–417 (1998).
9. V. Heine, *Group Theory in Quantum Mechanics* (Dover, New York, 1993).
10. O. Painter, K. Srinivasan, J. D. O'Brien, A. Scherer, and P. D. Dapkus, "Tailoring of the resonant mode properties of optical nanocavities in two-dimensional photonic crystal slab waveguides," *J. Opt. A, Pure Appl. Opt.* **3**, S161-70 (2001).
11. M. Tinkham, *Group Theory and Quantum Mechanics* (McGraw-Hill, San Francisco, Calif., 1964).
12. A. V. Oppenheim and R. W. Schaffer, *Discrete-time Signal Processing* (Prentice-Hall, Englewood Cliffs, N.J., 1989).
13. K. Sakoda, *Optical Properties of Photonic Crystals* (Springer, New York, 2001).
14. J. R. Cao, W. Kuang, Z. J. Wei, S.-J. Choi, H. Yu, M. Bagheri, J. D. O'Brien, and P. D. Dapkus, "Sapphire-bonded photonic crystal microcavity lasers and their far-field radiation patterns," *IEEE Photonics Technol. Lett.* **17**, 4–6 (2005).
15. J. D. Jackson, *Classical Electrodynamics* (Wiley, New York, 1962).